USE OF SATELLITE DATA FOR THE GENERATION OF SEA SURFACE TEMPERATURE CHARTS FOR MARINE FISHERY APPLICATIONS

Merritt R. Stevenson Consultant, Inter-American
Tropical Tuna Commission

For the past decade scientists in the United States have been launching meteorological satellites in the expectation and hope of gaining new understanding of global meteorological processes and through the development of new remote sensors placed aboard these successive satellites, to obtain for mankind greater ability to monitor present weather conditions and to predict weather conditions for the immediate future. Scientists in the field of oceanography have shown increasing interest during this period of development as the spatial resolution of the spaceborne sensors have been significantly improved.

Our discussion will deal with the particular aspects of the two-channel radiometers aboard NOAA satellites and how thermal infrared observations have been used and evaluated in several small studies, all aimed toward the generation of Sea Surface Temperature (SST) maps for use by marine fishery scientists. It should be stressed, however, that the computer techniques for processing the radiometer data for this particular use are no different than what would be used for the generation of other map products. Indeed, other oceanographic map products can be readily produced by modification of these computerized techniques.

Because of possible differences in background of the reader, we will first very briefly review the sensors that collected our data. In the first Figure we have a diagram of an early operational NOAA satellite. Note the location of the Scanning Radiometer. This instrument is designed to continuously scan a narrow swath from horizon-to-horizon on the earth's surface at right angles to the direction of orbital motion. The details of this instrument are best seen in Figure 2. The two-channel instrument utilizes visible (0.6-.7 micron bandpass filter) radiation and thermal infrared (10.5-12.5 micron bandpass filter) radiation collected with a common optical mirror. The analog voltage signals corresponding to changes in incoming radiation are then telemetered via a high frequency radio link down to earth where data acquisition stations in different countries can receive the data stream. Until a few years ago this was the primary sensor for obtaining surface temperature data from NOAA satellites.

Early studies involving thermal data from this sensor showed the inherent potential for using Scanning Radiometer InfraRed (SRIR) data in the area of fishery oceanography. In Figure 3 we see a sea truth comparison of SRIR Black Body equivalent temperatures (T_{bb}'s) and the occurrence of albacore tuna caught about 1,800 km west of the coast of California (Stevenson and Miller 1974). Surface temperatures taken from the R/V JORDAN (Laurs and Associates 1973) were compared to the SRIR temperatures and after allowance was made for atmospheric absorption of SRIR measurements due to atmospheric moisture, the two temperatures corresponding to the maximum catch were found to differ by less than 0.5°C! Other similar fish catch and SRIR temperature correlations described by Stevenson and Miller (1974) showed similar promise. This work was followed by later studies by IATTC scientists (Stevenson and Miller 1975) where tuna vessel locations were superimposed on SRIR derived SST maps such as shown in Figure 4. Generally tuna vessels fish in or near thermal fronts or interfaces where cool and warm water eddies may occur. While the first several years of Commission research with SR data showed the scanning radiometer to be capable of providing reasonably reliable temperature data, several problems discouraged the continued use of these data. The greatest limitation to the SR data is its 8-9 km (optimum) spatial resolution. While this may not be important in the open ocean, the magnitude of this uncertainty in location becomes very important in coastal fishing zones which may be only 90-200 km in width. Other shortcomings involve the problem of cloud contamination and uncertainties in absolute geographic location of the SR data. SR data can be used for various regional oceanographic studies however, such as a recent study using GOSSTCOMP data; the results will be presented at this Symposium (as IV.b.6; Ikeda and Stevenson 1978), where important climatological and oceanographic information can be extracted for a spatial scale larger than that limited to a narrow coastal zone.

Several years ago NOAA decided to begin a second family of scanning radiometers possessing much greater spatial resolution and this instrument was called the Very High Resolution Radiometer (VHRR). Its general design was similar to the SR but the primary optical mirror was much larger in order to provide a spatial resolution of about 0.9-1.0 km. Certain aspects of the VHRR were changed from the SR such as the rate of mirror rotation to accommodate the much higher data acquisition rate. Data acquisition stations also had to have larger and more sophisticated tracking equipment. Figure 5 shows the improved spatial and thermal resolution possible with the VHRR system in a view of the California coast. Commission scientists, shortly after the implimentation of VHRR systems, began to experiment with VHRRIR data and to develop programs to

handle the much larger data arrays corresponding to relatively small geographic regions. In Figure 6 we have taken about 20,000 VHRRIR observations converted them into T_{bb} temperatures and compensated for atmospheric effects and attempted to geographically grid the resulting computer contoured SST map (Stevenson and Miller 1975). Both Figure 6 and Figure 4 are for the same date, November 12, 1974. Even this early VHRRIR SST map shows the possibilities of detecting cooler surface plumes of water resulting from localized coastal upwelling. Because of the higher data rate and improved spatial and thermal resolution, certain data processing problems became even more significant and these will be discussed.

An important part of all sea truth experiments with satellite data is to provide surface "truth" data. This can be done by taking surface temperatures with bucket thermometers, by using data from Nansen bottles or a thermograph or possibly by using a Precision Radiation Thermometer (PRT) suitably mounted on a ship's superstructure and pointed downward toward the sea surface. Since the PRT instrument works on the same electromagnetic principle as the VHRR instruments aboard satellites, some scientists consider the use of PRT sea truth data best for calibration of satellite data. Figure 7 shows a simple statistical analysis of PRT and bucket temperature data (Stevenson, Miller and Kirkham 1976). The scatter present represents the difference in measuring the uppermost water film temperature and the water temperature in the upper meter of water.

To most users of VHRR data the conversion from raw digital engineering units (bytes) into nominal T_{bb} (in $^{\circ}K$ or $^{\circ}C$) values, represents a considerable problem. The method in general use starts with the calibration data collected during each scan of the VHRR mirror system and results in data of the type shown in Table I (Stevenson and Kirkham 1977).

TABLE I. VHRR Calibration Data for Orbit 4395

Quantity		Digital Count
C(sp)	(space view)	32
C(0)	(wedge 0, 0V)	241
C(1)	(wedge 1,-1V)	205
C(2)	(wedge 2,-2V)	170
C(3)	(wedge 3,-3V)	133
C(4)	(wedge 4,-4V)	98
C(5)	(wedge 5,-5V)	62
C(6)	(wedge 6,-6V)	26
C(ir)	(calibration target view)	161
C(T1)	(thermistor 1)	161
C(T2)	(thermistor 2)	158

A voltage step wedge designed to cover the thermal dynamic response of the instrument is scanned each rotation of the mirror and provides Digital Count or Number values that correspond to output voltages by the sensor system. In addition to this wedge, two onboard thermistors are scanned which provide voltage data on the housing temperature of the VHRR detectors. This is necessary because the thermal response of the VHRR system is temperature dependent; that is, the thermal sensitivity of the VHRR detectors changes with temperature changes of the IR detectors. Compensation for this ever present instrument problem provides much more stabilized data than would otherwise be possible. The step wedge information is combined with the thermistor information to provide sufficient data to compute algorithms relating DN's to voltages. To relate the energy received by the VHRRIR detectors with temperature ($^{\bullet}K$), it is necessary to make use of Planck's radiation equation (Stevenson and Kirkham 1977):

$$E_{\lambda}(T) = \frac{2hc^{2}}{\lambda^{5}\left[\exp\left(\frac{hc}{\lambda kT}\right) - 1\right]}$$ where

$h = 6.626 \times 10^{-34}$ joule-sec (Planck constant)

$c = 2.998 \times 10^{10}$ cm/sec (speed of light)

$k = 1.381 \times 10^{-23}$ joule/$^{\bullet}K$ (Boltzman constant)

We will not go into the theory that gives rise to the equation but only explain its usefulness in converting black body radiation of a specific wavelength and temperature into equivalent energy. Since the amount of energy received is the total of the different wavelengths falling upon the infrared sensor, knowledge of the IR bandpass filter used in the VHRR system is important. Figure 8 (Stevenson and Kirkham 1977) shows the spectral response of this filter, for example $\overline{\lambda} = 11.5$ microns. This wavelength is inserted into the above equation to obtain the energy corresponding to that wavelength. There is still a problem, however, in that the desired temperature T is still an unknown in the equation. By the use of the engineering data and calibration end-points such as space temperature measured by the radiometer during each scan, we can obtain the intermediate equations (Stevenson and Kirkham):

$$E_{\lambda}(C_{sp}) = mC_{sp} + b$$

$$E_{\lambda}(C_{ir}) = mC_{ir} + b$$ where C_{sp} and C_{ir} are given in Table I and m and b are slope and intercept of the generalized form of this linear equation. From here we go back to the radiation equation and invert the equation to obtain the solution in terms of absolute temperature to

obtain:

$$T = \frac{hc}{k\lambda \ln\left[\frac{2hc^2}{\lambda^5 E_\lambda} + 1\right]}$$

Because of the time required to evaluate each DN value in a data array, these equations form part of an overall computerized system to process satellite data.

The next problem to be considered is that caused by atmospheric attenuation or limb darkening. To accomplish this we need consider the geometry of how the VHRR scans the earth's surface. In Figure 9 we see the elements of importance including the nadir angle η and the zenith angle θ (Stevenson and Kirkham 1977). The resulting equation relates the desired zenith angle to the known nadir angle of the scanning mirror of the VHRR system as follows:

$$\theta = \text{arc sin}\left[\frac{H + R}{R} \cdot \sin\eta\right]$$

Once we have this relationship we can go to a semi-empirical equation developed by Koffler (1976) at NESS/NOAA and given as:

$$\Delta T = (-26.81 + 0.1072\ T_{bb})\ \exp\ (0.000120^2)$$

This value must be added to the calibrated T_{bb} value to obtain the corrected calibrated temperature. This equation is based on a number of test areas and latitudinal zones and relates the attenuation to the change in zenith angle (in degrees) or change in path length through the atmosphere between the footprint seen by the sensor and the sensor itself. The algorithm provides a good correction to the nominal T_{bb} values assuming normal temperature and moisture profiles to be present in the target area.

The next problem has to do with the spherical shape of the earth and how the VHRR scans this surface. There is negligible error when the sensor scans directly beneath the satellite's track but the error becomes appreciable as the scanner looks at the earth with increase in oblique angle. The effect is referred to as foreshortening and its impact on the location of data elements is easily seen in Figure 10 (Stevenson and Kirkham 1977). Within 400 km of the subpoint there appears to be little error but when the scanner is looking 1400 km from the vertical the positional error becomes 200 km, very significant in data possessing spatial resolution of 2-4 km. The resulting algorithm is used in relocating coordinate grid points for the data array and will not be further discussed here.

We now have our VHRR data converted into T_{bb} values ($^\circ$K or $^\circ$C) and corrected for moisture under clear sky conditions. A gridding scheme is next used to provide geographic reference and the data are then ready for use. Clouds present in the data field still present a problem and require some

knowledge of the nature of cloud cover and water vapor in the lower marine atmosphere in order to be fully evaluated. A recent study by Stevenson,Kirkham and Madsen (1977) discusses the problems inherent in screening out clouds. For our purposes the effect of including cloud contaminated data elements in our array of sea surface temperatures is seen in Figure 11 (Stevenson and Miller 1974). These data were taken from an SR system but the effect is the same for the VHRR sensor, namely a bias toward colder temperatures when using these contaminated values. In Figure 12 we see the problem in more detail (Stevenson Kirkham and Madsen 1977). Both the temperature and moisture profiles are seen from the surface to an altitude of about 9 km, above the marine layer. Where the water vapor forms an appreciable opacity to the sensor (both the IR and VIS channels) at that altitude, the sensor will be biased toward the temperature and albedo at that altitude. Since the energy received by the VHRR radiometer is a sum of all outgoing radiation within the viewing angle of the sensor, knowledge of the height, and hence of the temperature of the appreciable vapor, becomes very important.Figure 13 shows this information in regard to integrated water vapor (Stevenson, Kirkham and Madsen 1977). Information provided by radiosondes taken within the area of interest can provide this information and will give rise to even better corrections for atmospheric moisture. The VTPR instrument aboard NOAA class satellites can, in principle, be used to provide this information where radiosondes are not available.

Thus far we have described techniques needed to convert raw VHRR data into usable temperatures. Because of the complexity and speed with which this must be done in order to have the results available in a timely fashion, it is necessary to have a data processing system to effect an efficient flow of information for this purpose. Figure 14 (courtesy David McConaghy,NMFS,La Jolla California) shows in general how such data were processed about a year ago by Commission scientists.

Interest by NMFS scientists at the Southwest Fishery Center in La Jolla California to utilize this system have resulted in the training of NMFS staff so that the SWFC now has a quasi-operational capability to process VHRR data on a weekly or near-daily basis. Several of the following figures were provided courtesy Lt. David C. McConaghy at NMFS (La Jolla) and is an example of how they are now proceeding to implement the technology developed by Commission scientists.

Two studies will be considered, the first occurred during April 19-21 1977. Figures 15 and 16 show the VHRR imagery used in the study. Note that the coastal zone is clear in the VIS channel but shows definite thermal gradients in the IR channel. The next figure shows a sample of the calibrated IR channel with

geographic coordinates and CalCOFI stations superimposed on the VHRRIR array. Table II shows the location accuracy possible for this study.

TABLE II. NOAA-5 Orbit 3268 Gradient Area 1; April 19, 1977

	DIGITAL IMAGE		MAP			
STATION	LAT	LNG	LAT	LNG	ΔLAT	ΔLNG
Trinidad Head	41.08	124.12	41.07	124.16	0.01	-0.04
Cape Mendocino	40.42	124.36	40.44	124.40	-0.02	-0.04
Punta Gorda	40.24	124.33	40.25	124.37	-0.01	-0.04
Punta Delgada	40.02	124.08	40.02	124.07	0.00	0.01
Cape Vizcaino	39.75	123.88	39.72	123.83	0.03	0.05
Fort Bragg	39.46	123.86	39.45	123.82	0.01	0.04

$$\Delta LAT = \sum_{n=1}^{6}\left(\frac{LAT_n}{n}\right) = 0.02^{\bullet} \qquad \Delta LNG = \sum_{n=1}^{6}\left(\frac{LNG_n}{n}\right) = 0.04^{\bullet}$$

The largest error was typically 4 km or less. The Coast Guard overflight occurred in the area two days later, on April 21. The SST map, made from PRT-5 data (Stevenson and Kirkham 1977) is seen in Figure 18. A comparison of overflight data with the VHRR averaged data is shown in Table III.

TABLE III. NOAA-5 Orbit 3268 Gradient Area 1; April 19, 1977

STATION NO.	LAT(°N)	LNG(°W)	T_{st}(°C)	T_{NS}(°C)
1	40.77	124.48	8	10
2	40.75	124.66	9	11
3	40.65	125.34	10	12
4	40.04	125.30	10	12
5	40.09	125.06	9	11
6	40.15	124.78	8	11
7	40.20	124.60	8	10
8	39.80	124.36	9	11
9	39.75	124.52	10	12
10	39.72	124.63	10	12
11	39.66	124.82	9	11
12	39.57	125.14	9	11
13	39.37	125.41	10	12
14	39.28	124.12	10	11
15	39.30	124.08	9	11

Std. Dev. of ΔT = 0.38 °C

The data pairs show a mean temperature offset of 2°C of the surface PRT-5 measurements and r = 0.87 which is good, considering the time lag of two days. In order to adequately match the data sets, the several pixels surrounding "ship station" locations were averaged; in this instance 3 pixels each on 5 scanlines centered about the station position are averaged to obtain a representative T_{bb} value. This is done to guarantee that the satellite observations overlap each "ship station".

Using the 48" X 48" computer printout format, data arrays can be presented for 3 scaled views. The full view contains an area of approximately 500 n.mi. X 500 n.mi. (928 km X 928 km). While the view is panoramic, there is

considerable VHRR data compression - 15:1 along a scanline and 3:1 along track. For the medium view the field is about 140 n.mi. X 140 n.mi. (260 km X 260 km). The data compression becomes 5:1 along scanline with no compression along track. For the full resolution the region covered reduces to about 32 n.mi. X 32 n.mi. (or 60 km X 60 km). There is no compression along scanlines and in order to retain the proper aspect ratio data between scanlines must be interpolated. Figure 19 is a medium view for April 19, 1977. Instead of showing hand contoured isotherms we show here a simple computerized gray scaled contouring of the sea surface temperature at 1°C contour intervals. Note that the patterns are relatively smooth and are in fact due to using a two-dimensional smoothing function on the data field to suppress high frequency noise present in the medium resolution view (Stevenson and Kirkham).

It seems now that a sensor of sufficient accuracy and spatial resolution and that is reasonably free of technological problems is now available for use by scientists of the marine community. Uses of this Very High Resolution Radiometer data by marine fishery scientists, oceanographers and others, is only limited by our imagination and willingness to develop the necessary numerical techniques.

REFERENCES

Ikeda, Yoshimine and Merritt Stevenson. 1978. Time Series Analysis of NOAA-4. Remote Sensing of Environment. 7:349-360.

Koffler, Russell. 1976. Digital Processing of NOAA's Very High Resolution Radiometer (VHRR) Data. International Astronautical Federation, 27th Congress, Ref. No. 76-209.

Laurs, R. Michael and Associates. 1973. Report of Joint National Marine Fisheries Service - American Fishermen's Research Foundation Albacore Studies Conducted During 1973. Unpublished Report, National Marine Fisheries Service, Southwest Fisheries Center: 65 p.

Stevenson, Merritt R. and Forrest R. Miller. 1974. Application of Satellite Data to Study Oceanic Fronts in the Eastern Pacific. Inter-American Tropical Tuna Commission. Final Report for SPOC, NOAA Grant No. 04-3-158:111 p.

_____. 1975. Application of Satellite Data to Problems in Fishery Oceanography. Final Report for SPOC, NOAA Grant No. 04-4-158: 98 p.

Stevenson, Merritt R., Forrest R. Miller and Robert G. Kirkham. 1976. Comparison of NOAA 3-4 VHRR Imagery and LANDSAT Multi-Spectral Scanner Images with Marine Resource Measurements. Inter-American Tropical Tuna Commission. Final Report for SPOC, NOAA Grant No. 04-6-158-44043: 111 p.

Stevenson, Merritt R. and Robert G. Kirkham. 1977. Coastal Zone and Open Ocean Observations from NOAA Satellite Very High Resolution Radiometers. Inter-American Tropical Tuna Commission. Final Report for SPOC/NMFS Contract No. 03-7-208-35236. 88 p.

Stevenson, Merritt R., Robert G. Kirkham and Bruce J. Madsen. 1977. Development and Testing of a Cloud Screening Technique for Use with Satellite-Borne Scanning Radiometers. Inter-American Tropical Tuna Commission. Final Report for Naval Environmental Prediction Research Facility. Grant No. N00228-76-C-3163. 95 p.

FIGURE CAPTIONS

1. A NOAA class polar orbiting satellite.

2. Optical schematic of the ITOS scanning radiometer (courtesy of Santa Barbara Research Center).

3. Comparison of albacore tuna catch rate and observed T_{bb} SRIR surface temperatures.

4. SRIR derived sea surface temperature field with tuna vessel locations for November 12, 1974.

5. Example of improved visual (left panel) and infrared (right panel) imagery available from the Very High Resolution Radiometer (VHRR) onboard NOAA class satellites.

6. Sea surface temperature (SST) map of a portion of the west coast of Baja California. Cooler plumes of surface water can be readily seen in upper central part of the figure.

7. PRT-5 calibration for June 1976 cruise.

8. Infrared channel relative spectral response of detector at 105°K, for NOAA-4 VHRR sensor #1.

9. Relevant geometry for defining the zenith angle, θ.

10. Graphical representation of physical effect of derived foreshortening algorithm.

11. Histograms of two adjacent SRIR surface temperature fields-one clear sky and one partly cloudy. Cloud contaminated histogram is displaced to colder temperature than clear sky histogram.

12. Profile of Air Temperature and Water Vapor Content, R/V JORDAN, 0144 GMT June 19, 1976.

13. Profile of Integrated Water Vapor for R/V JORDAN, 0144 GMT, June 19, 1976.

14. Computer program sequence for routine processing of VHRRIR data (courtesy David McConaghy, NMFS La Jolla).

15. VHRRVIS image for April 19, 1977 used in comparative study. Note absence of clouds near the California coast.

16. VHRRIR image for April 19, 1977 used in comparative study. Note the complex surface thermal gradients near the California coast.

17. Filtered medium area field derived from same raw temperature data as field field shown in Figure 19.

18. Sea truth isotherm field observed two days after NOAA-5 overflight.

19. Medium area grayscaled representation of Gradient region field for April 19, 1977. The temperature data are numerically filtered to minimize noise present in the data.

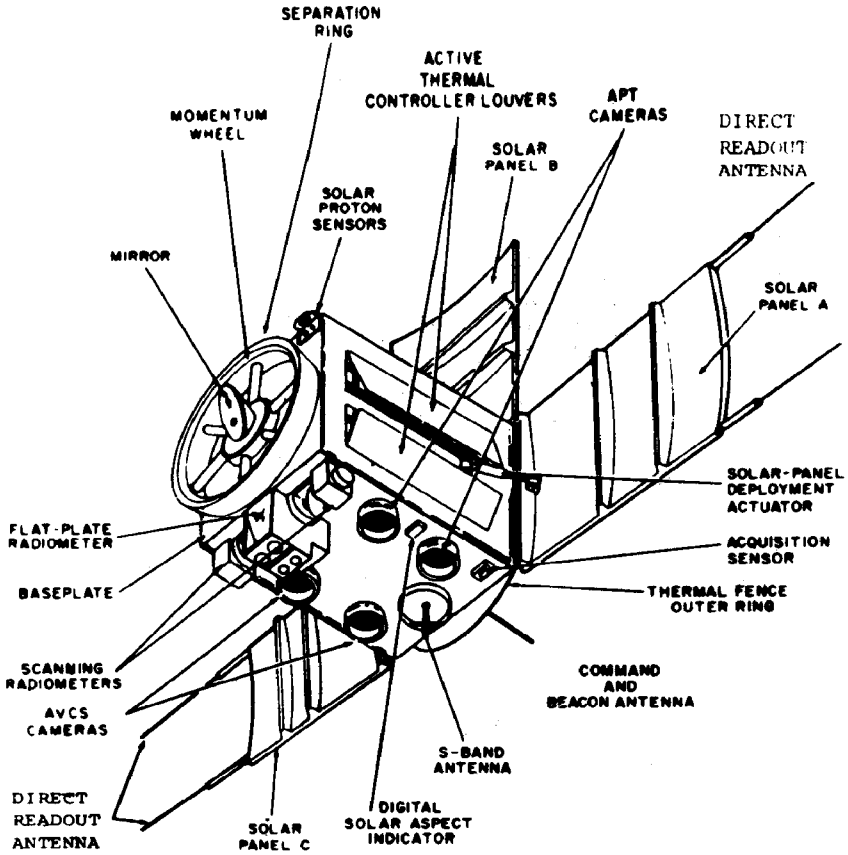

Figure 1 - The NOAA polar satellite.

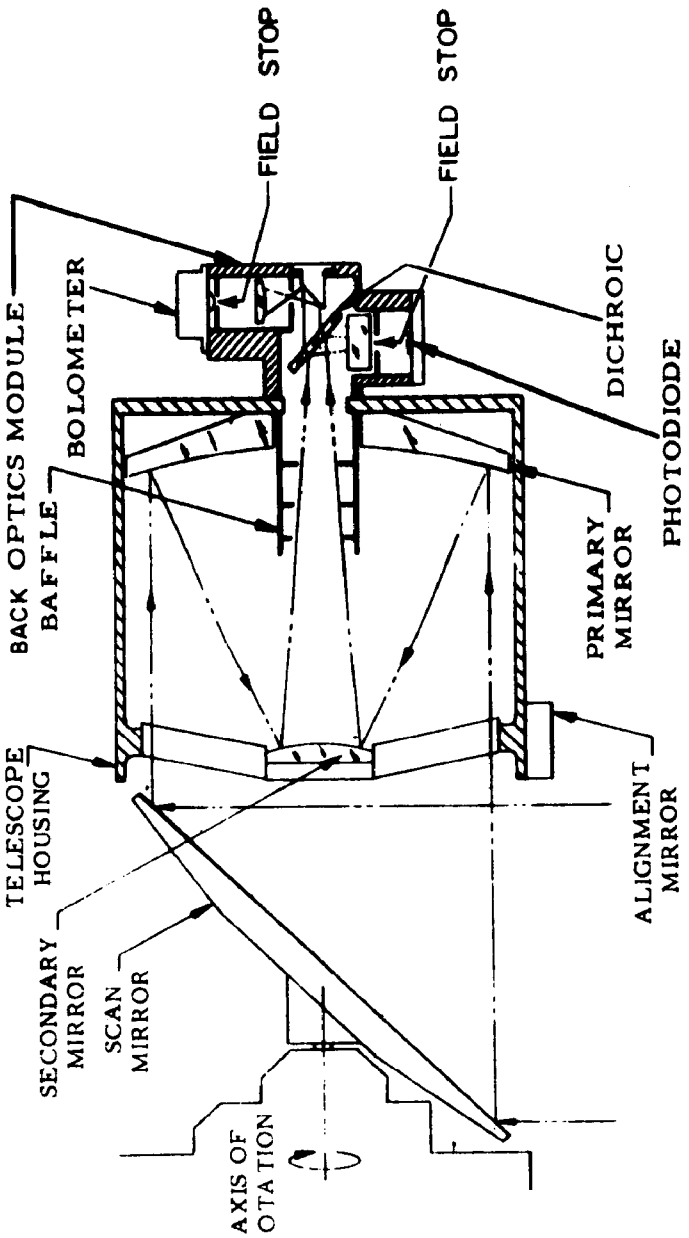

Figure 2 - Optical schematic, ITOS scanning radiometer.
(courtesy of Santa Barbara Research Center)

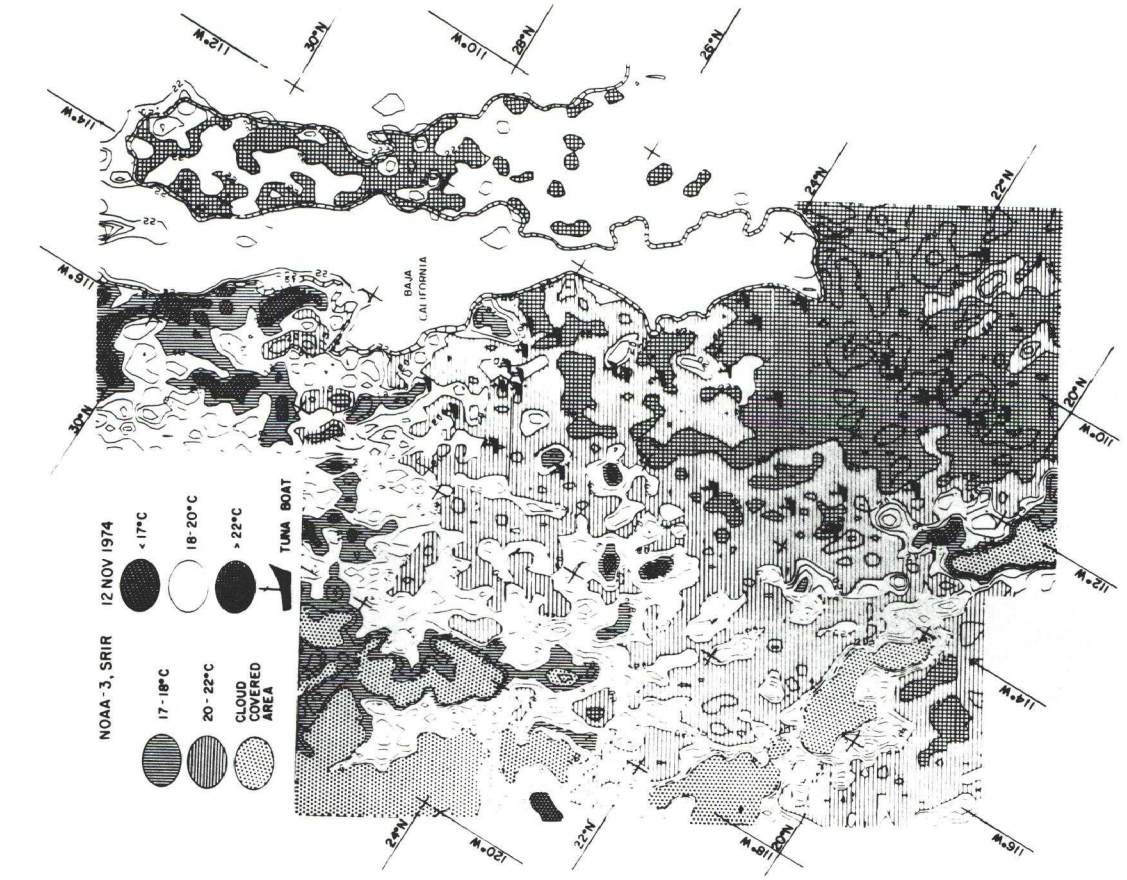

Figure 4

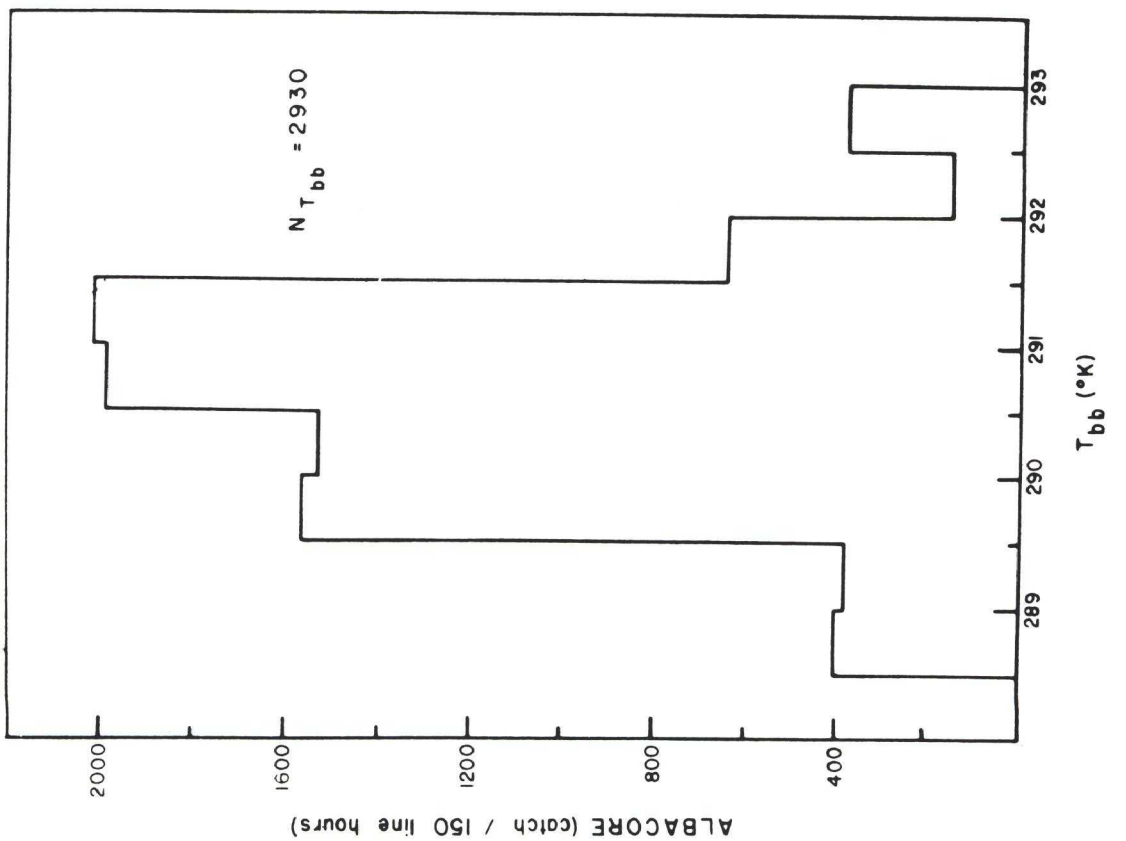

Figure 3

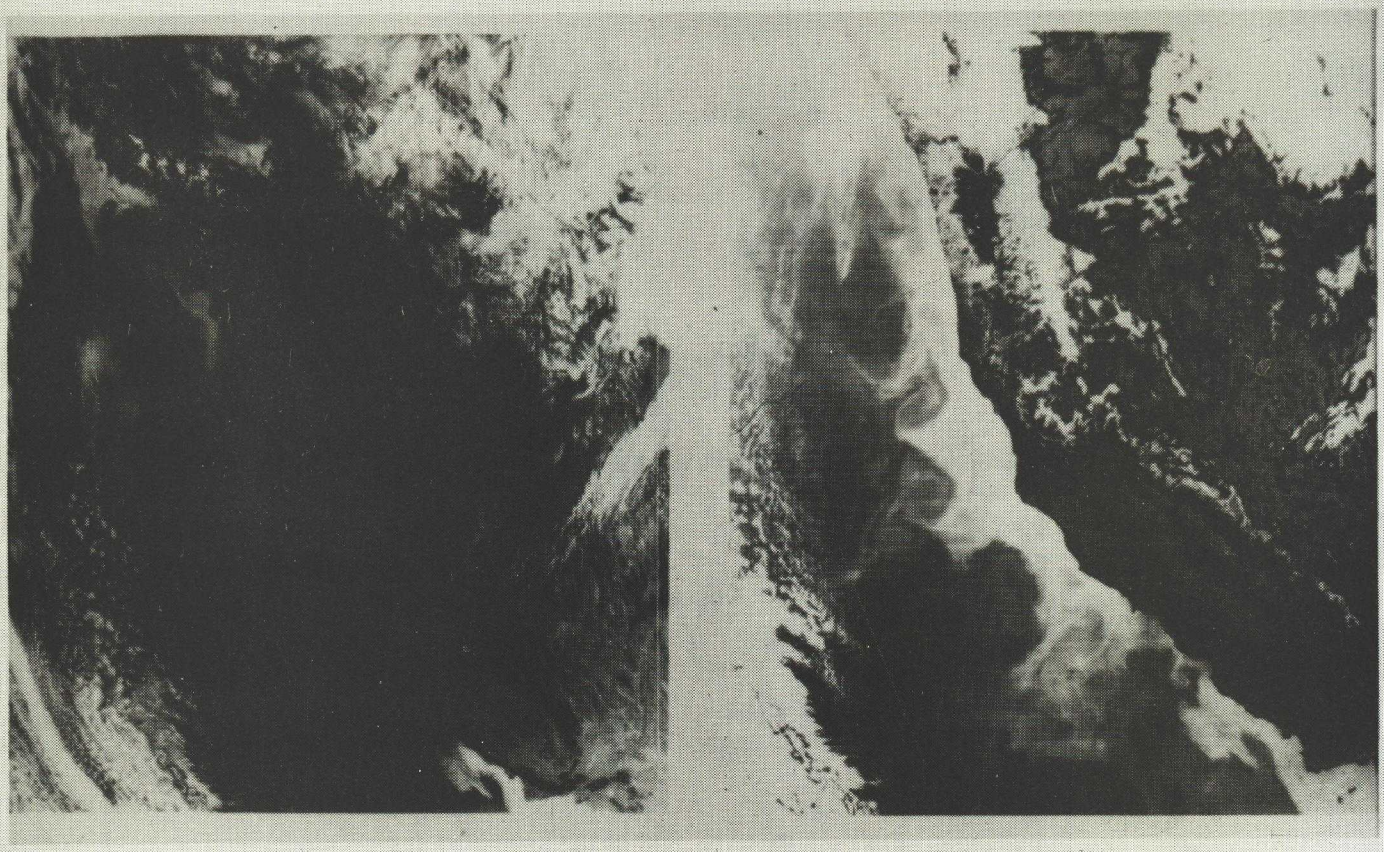

Figure 5

Figure 6

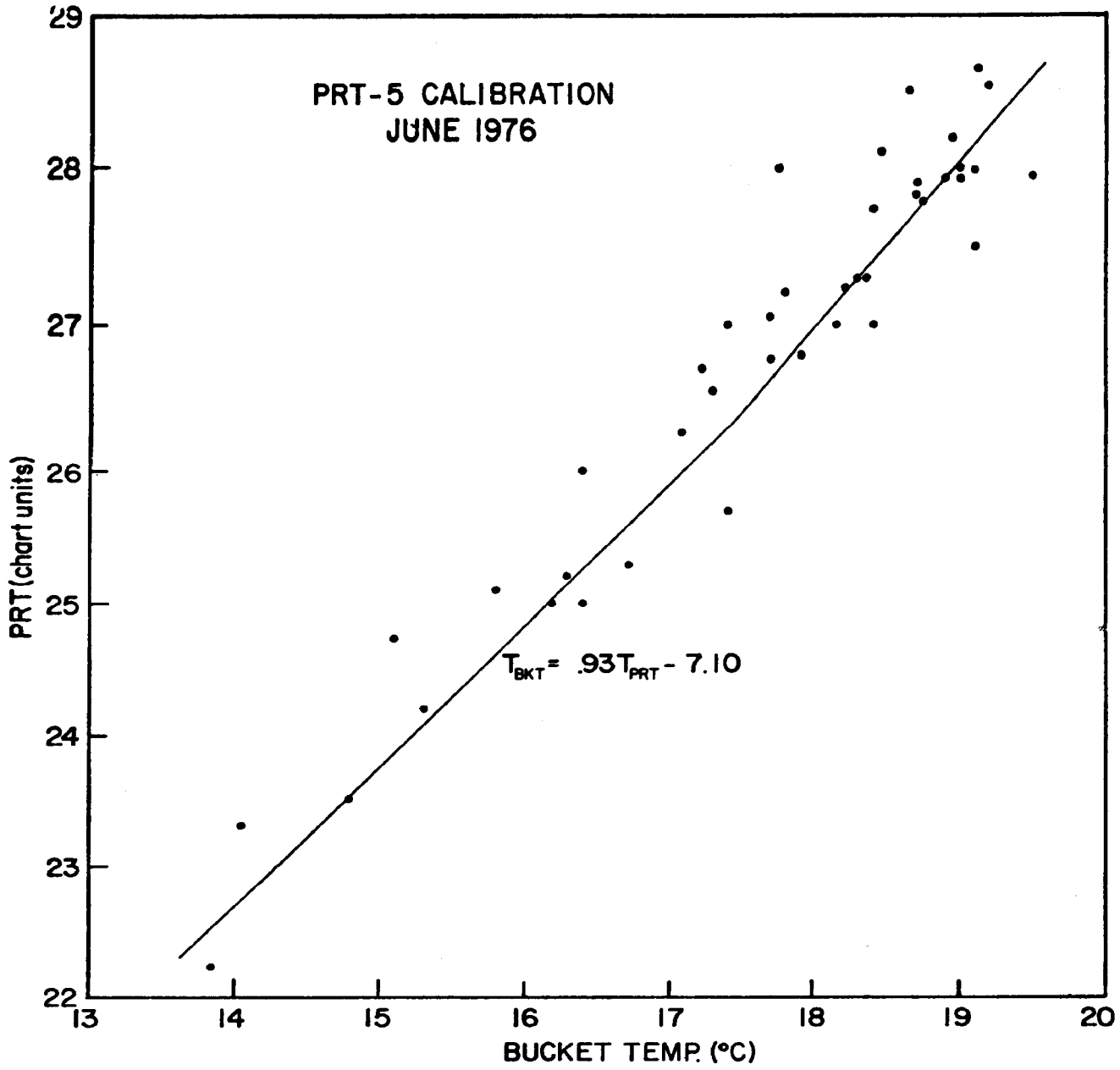

Figure 7 - PRT-5 Calibration - June 1976

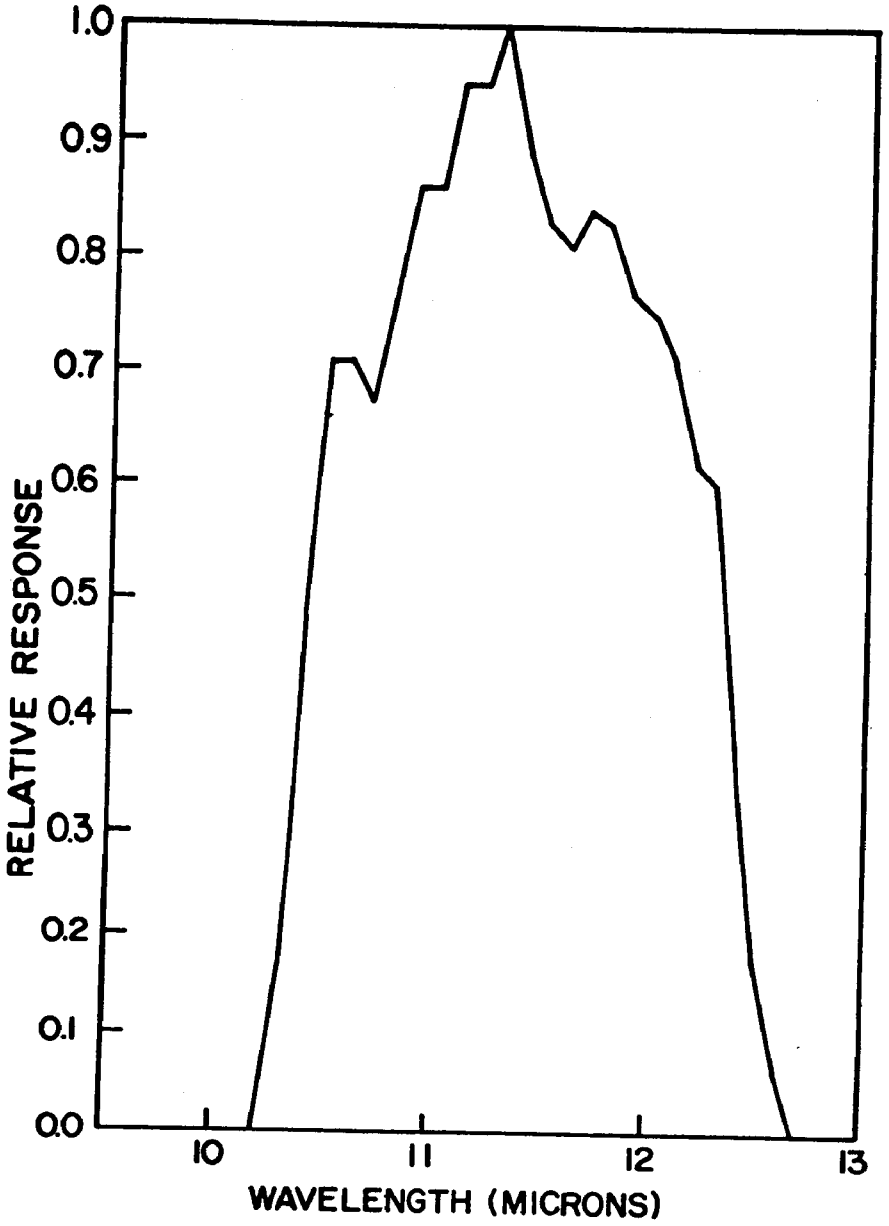

Figure 8 - Infrared channel relative spectral response detector at 105^{o}K, for NOAA-4 VHRR sensor 1.

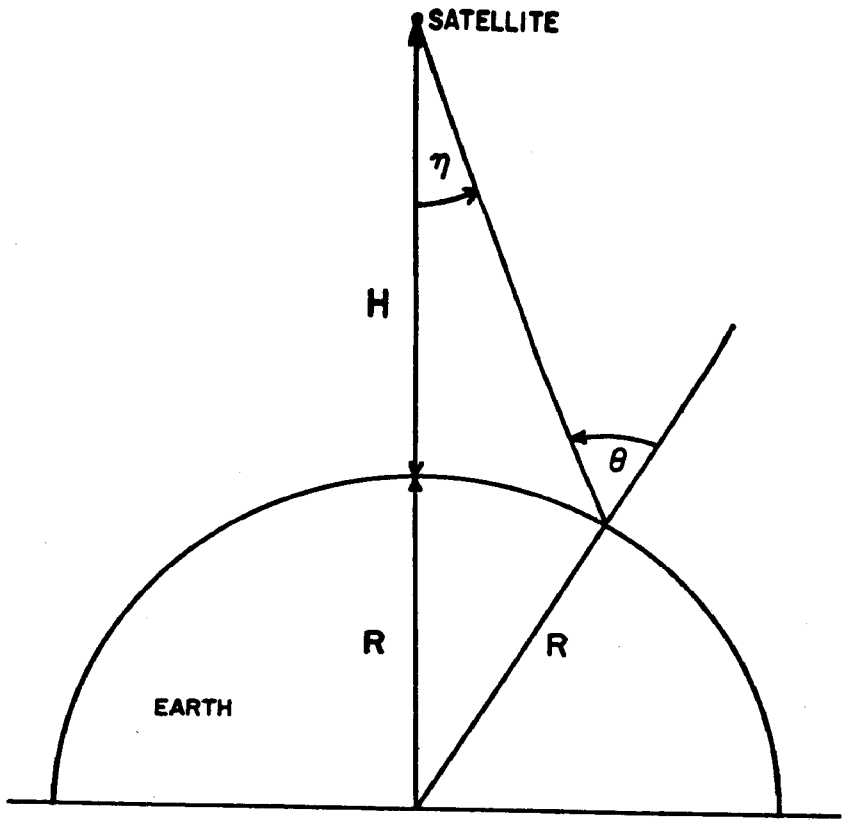

Figure 9 - Relevant geometry for defining the zenith angle, θ.

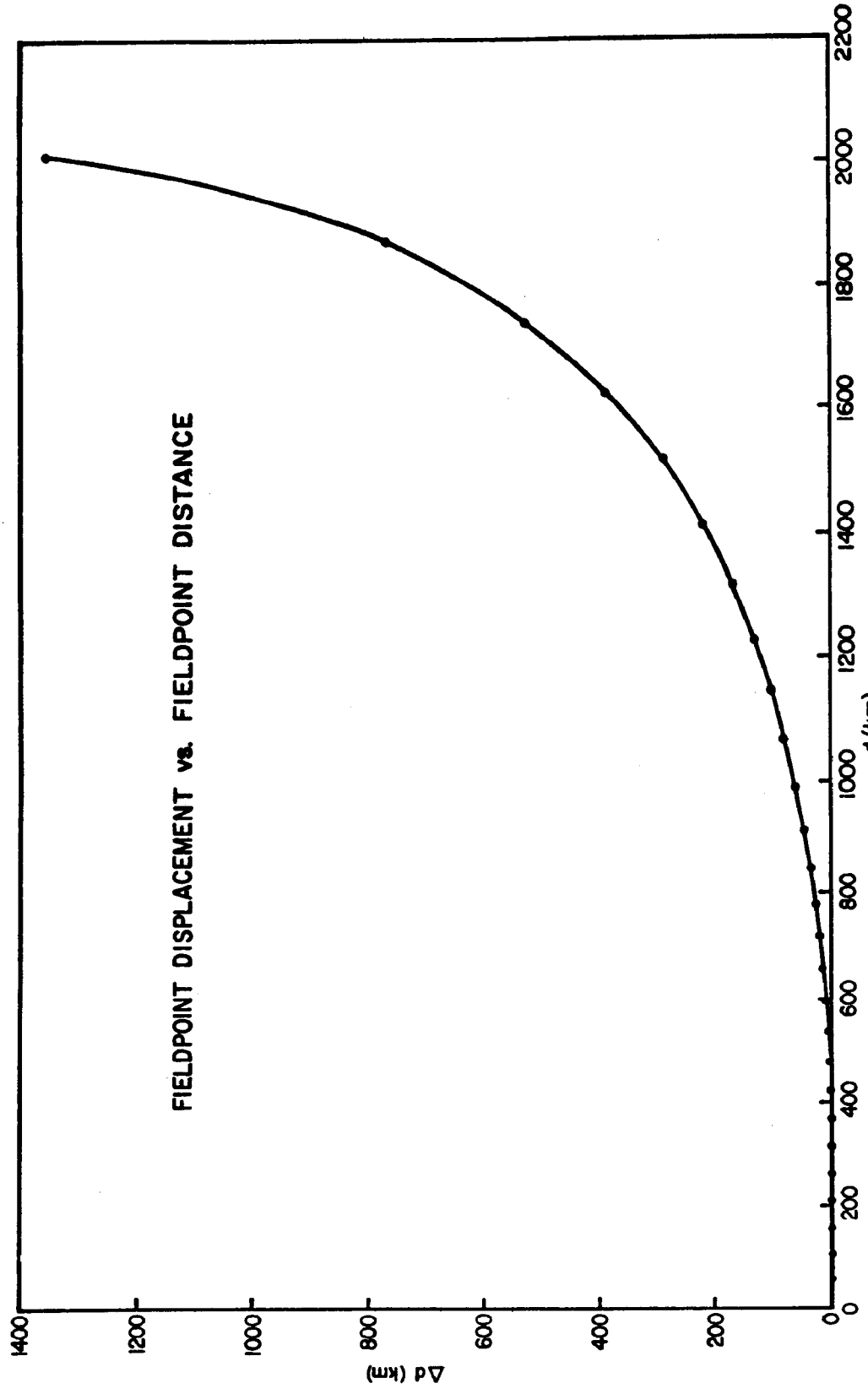

Figure 10 - Graphical representation of physical effect of derived foreshortening algorith.

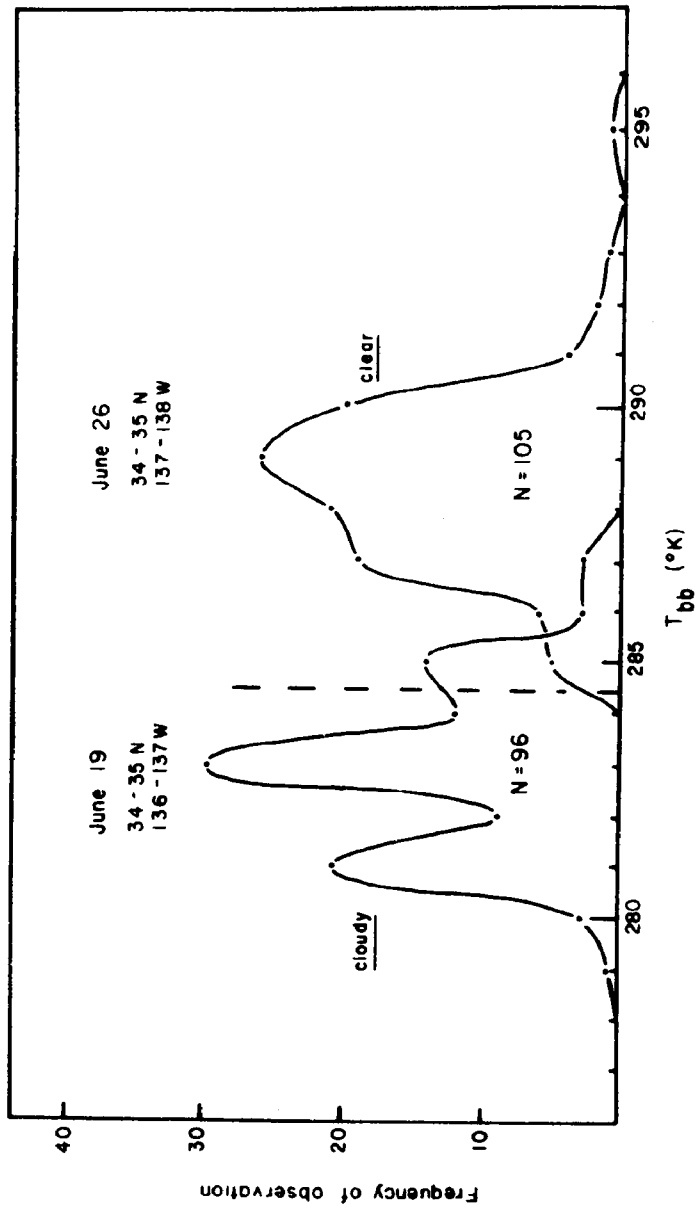
June 19
34 - 35 N
136 - 137 W
N = 96
cloudy
June 26
34 - 35 N
137 - 138 W
N = 105
clear
Frequency of observation
10
20
30
40
280
285
290
295
T_{bb} (°K)

Figure 11

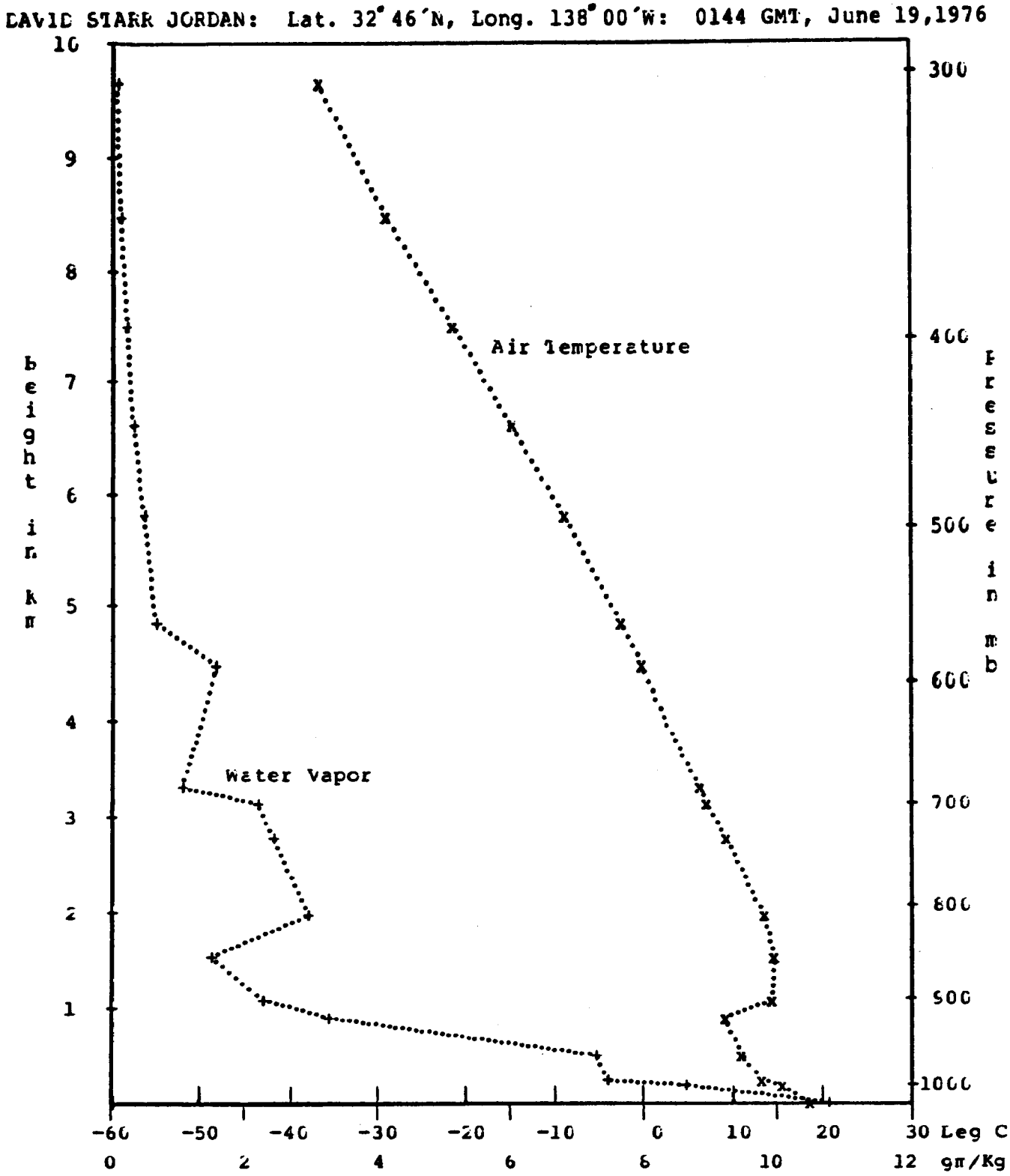

Figure 12 - Profile of Air Temperature and Water Vapor Content, R/V JORDAN, 0144 GMT, June 19, 1976.

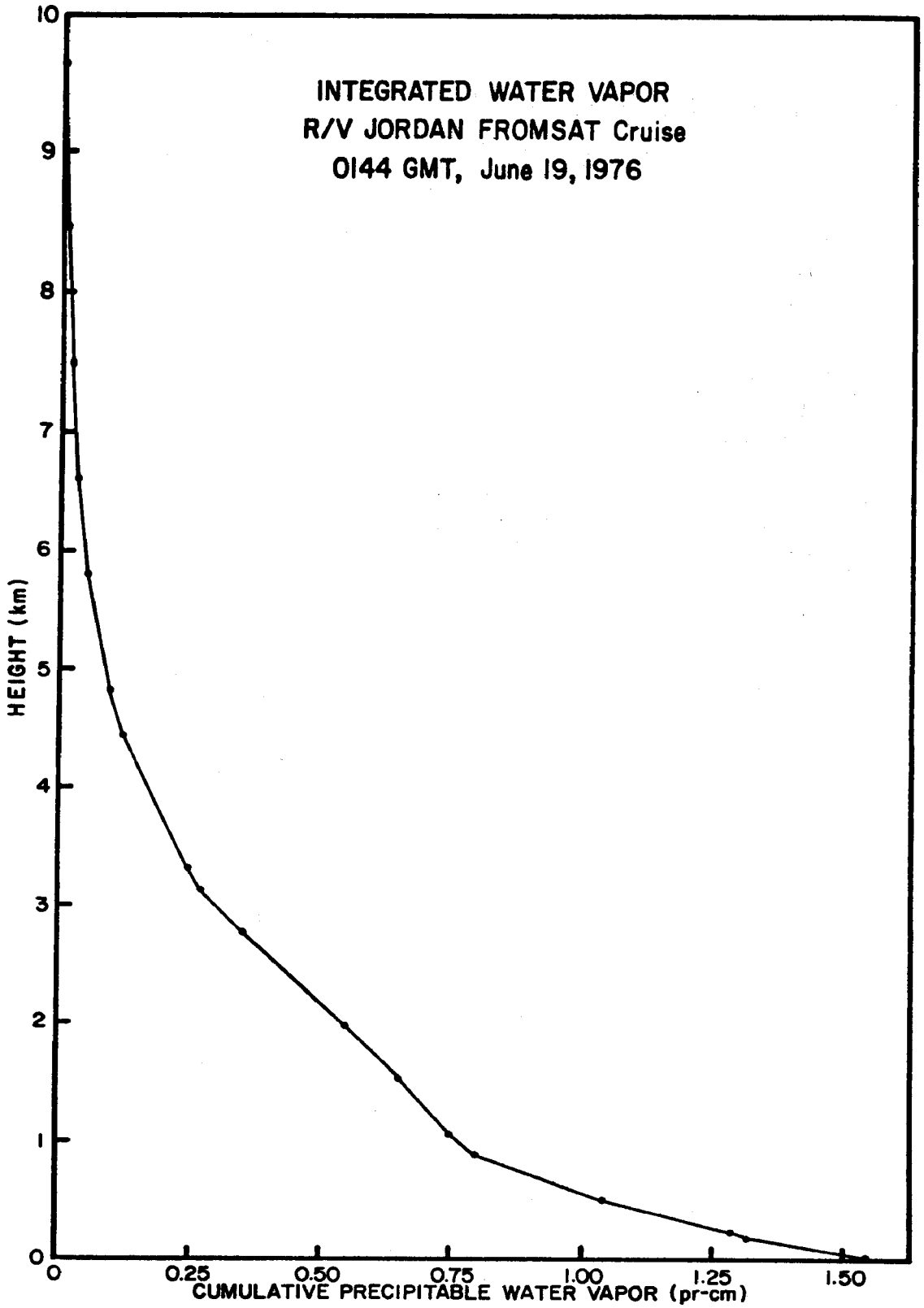

Figure 13 - Profile of Integrated Water Vapor for R/V JORDAN, 0144 GMT, June 19, 1976.

SATELLITE DERIVED SEA SURFACE TEMPERATURE
PROGRAM SERIES

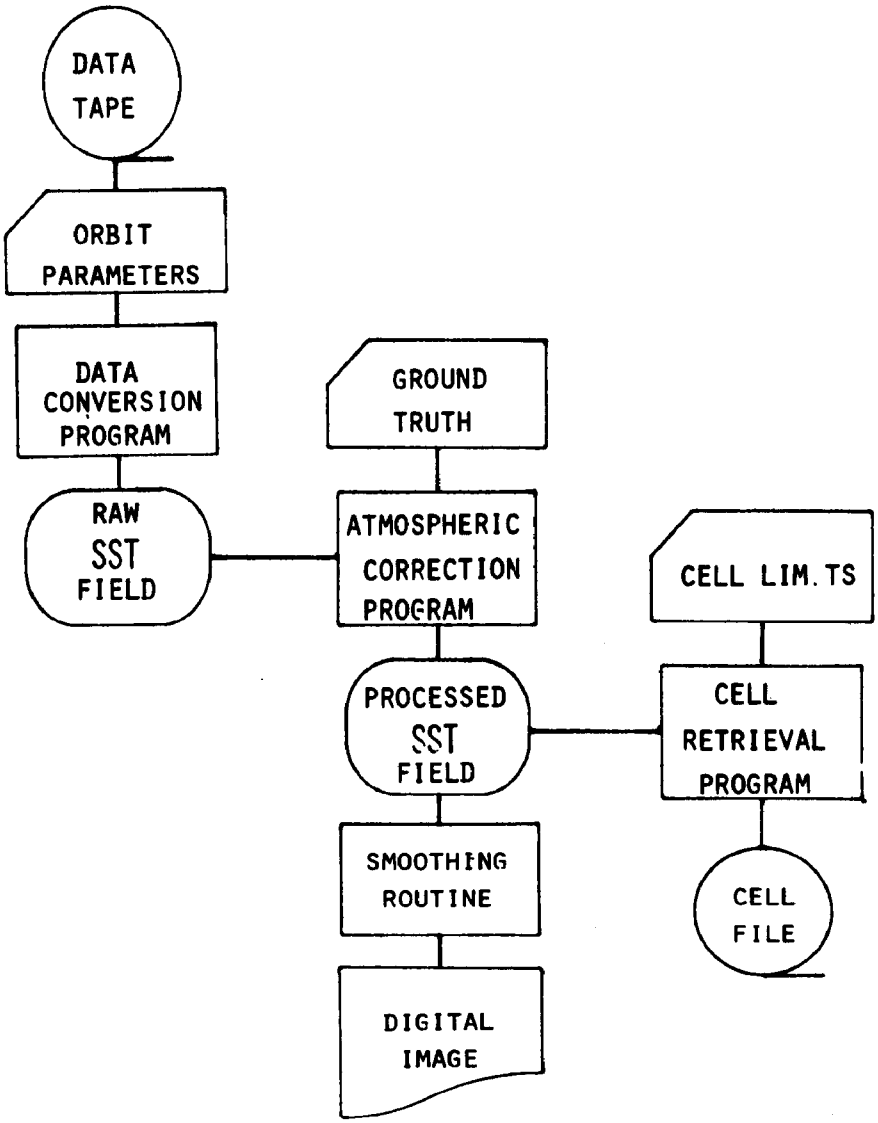

Figure 14

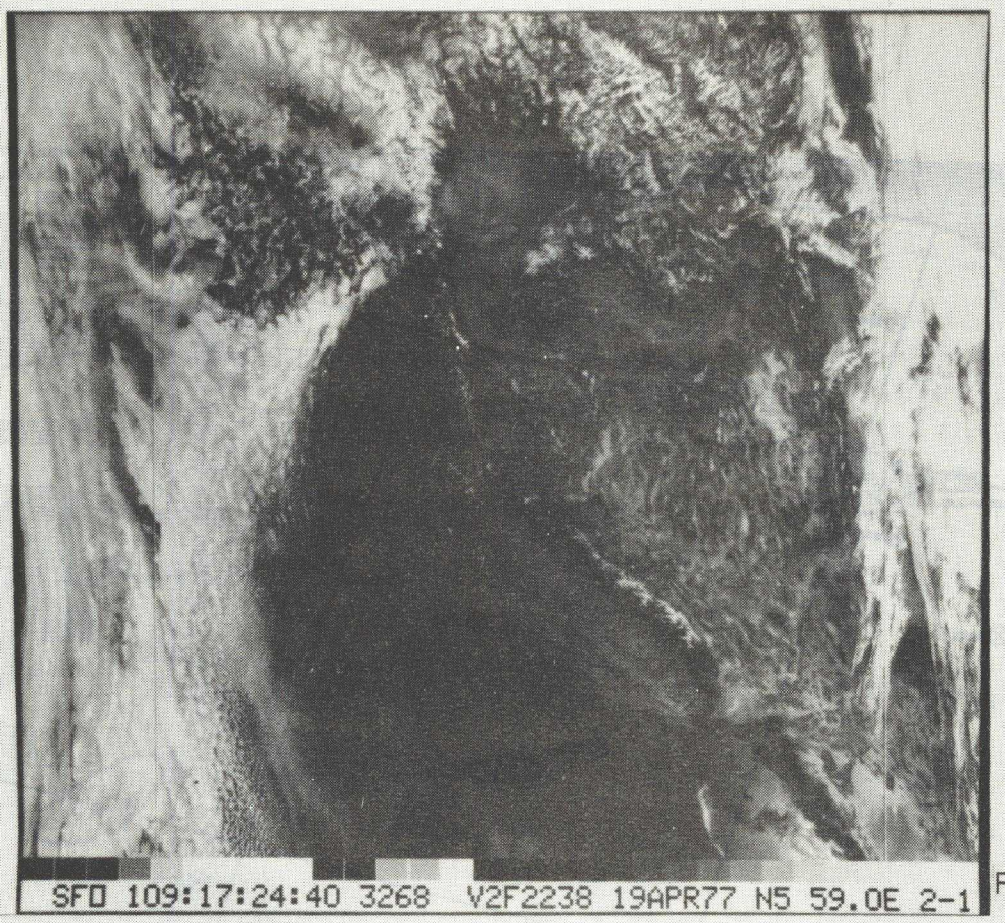

Figure 15

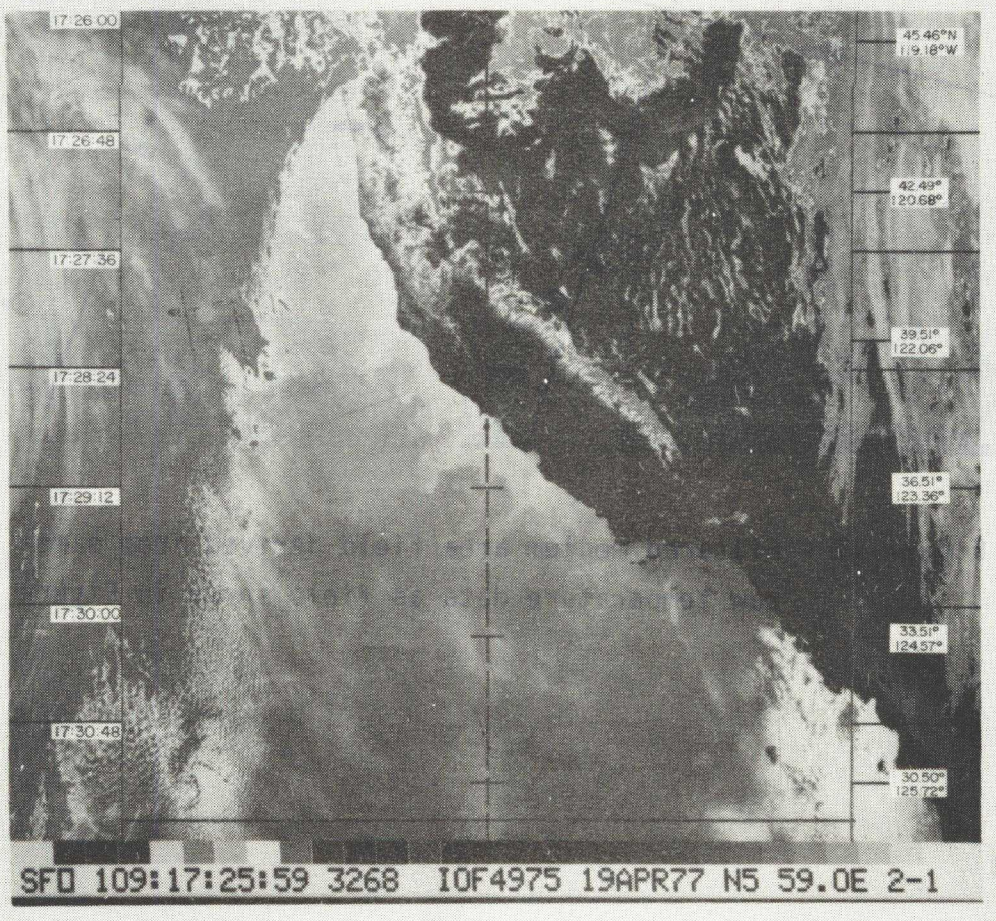

Figure 16

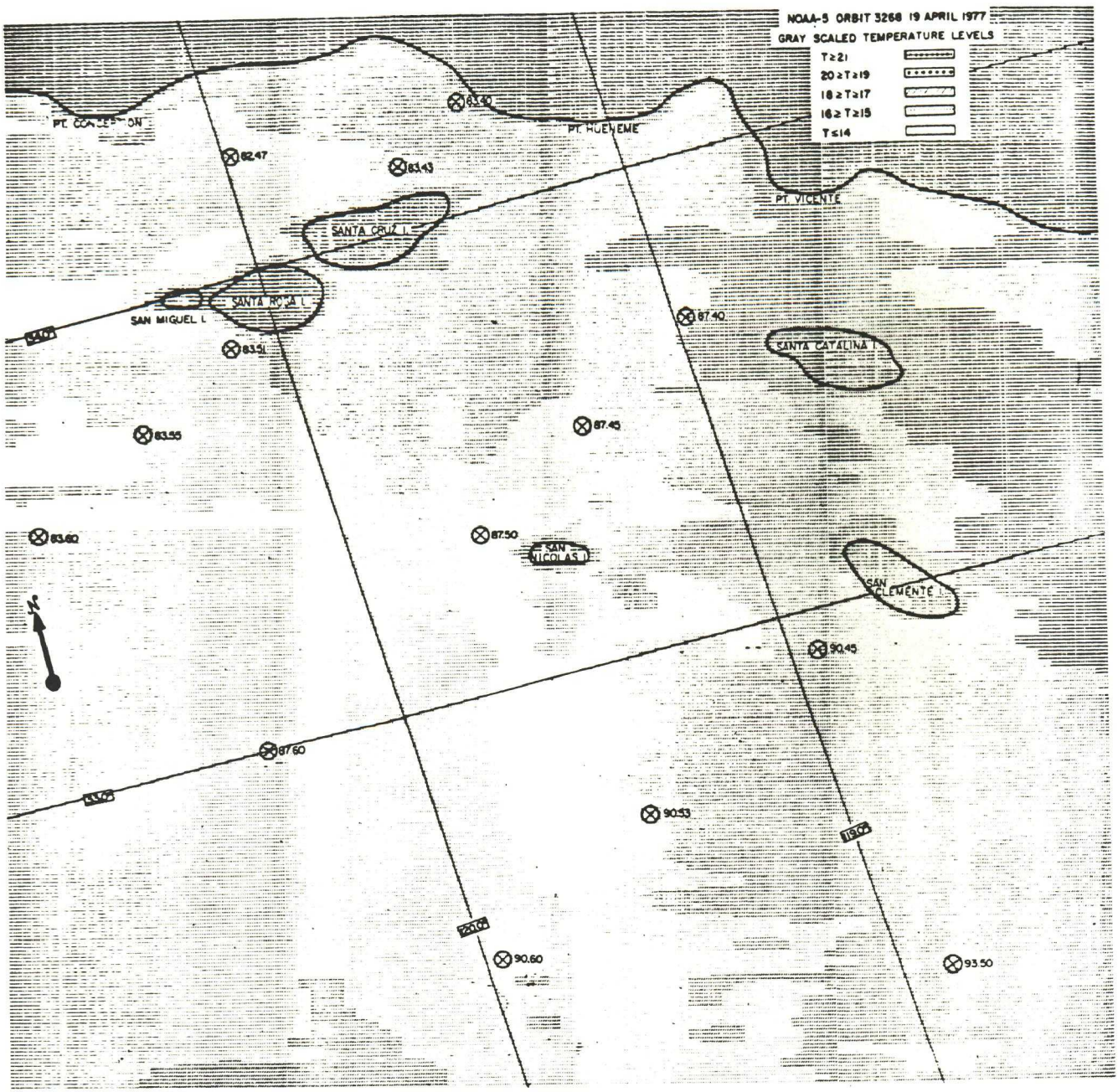

Figure 17 - Filtered medium area field derived from same raw temperature data as field shown in Figure 19.

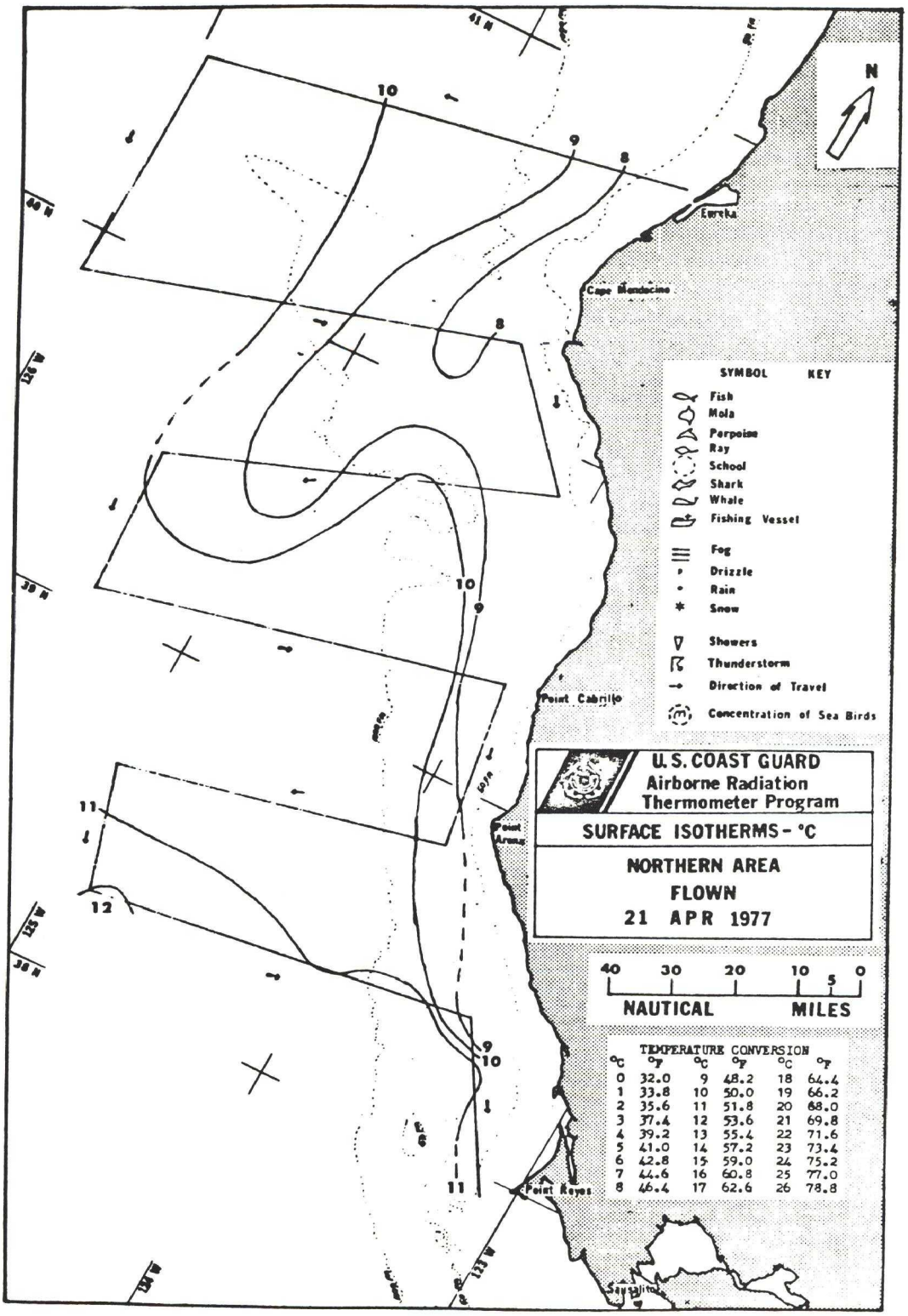

Figure 18 - Sea truth isotherm field.

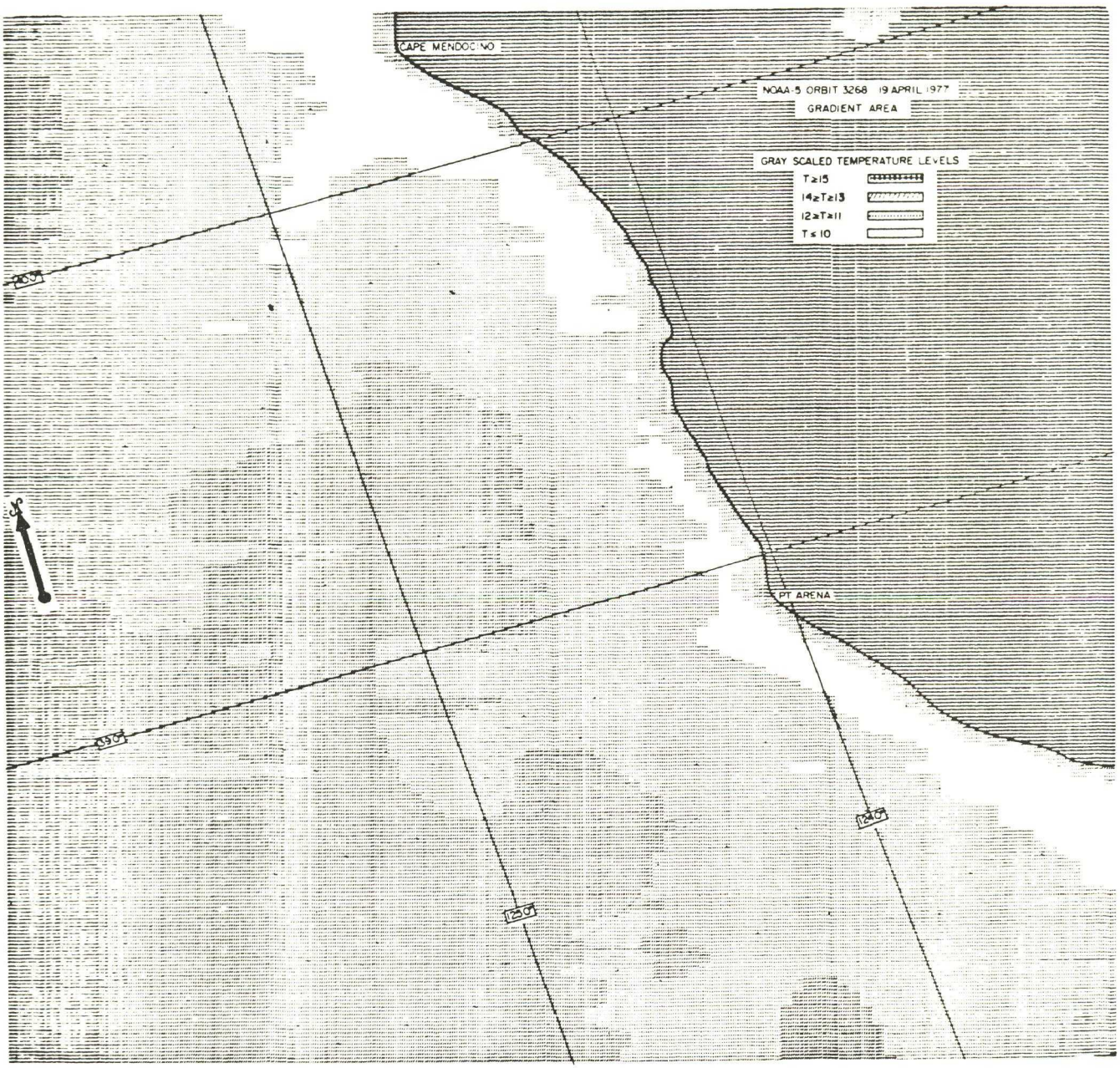

Figure 19 - Medium area grayscaled representation of Gradient region temperature field. Filtered.